MQGeometry-1.0: a multi-layer quasi-geostrophic solver on non-rectangular geometries

Louis Thiry[1], Long Li[1], Guillaume Roullet[2], and Etienne Mémin[1]

[1]ODYSSEY, INRIA Rennes, IRMAR Rennes, Université de Rennes 1, France

[2]Université de Bretagne Occidentale, CNRS, IRD, Ifremer, Laboratoire d'Océanographie Physique et Spatiale (LOPS), IUEM, Brest, France

Correspondence: Louis Thiry (firstname.lastname@inria.fr)

Abstract. This paper presents `MQGeometry`, a multi-layer quasi-geostrophic (QG) equations solver for non-rectangular geometries. We advect the potential voriticity (PV) with finite volumes to ensure global PV conservation thanks to a staggered discretization of the PV and stream-function (SF)~~,~~. Thanks to this staggering, the PV is defined inside ~~of~~ the domain, removing the need for defining the PV on the domain's boundary. We compute PV fluxes with upwind-biased interpolations whose implicit dissipation replaces the usual explicit (hyper-)viscous dissipation. The presented discretization does not require the tuning of any additional parameter, *e.g.* additional ~~hyper-viscosity~~eddy viscosity. We solve the QG elliptic equation with a fast discrete sine transform spectral solver on rectangular geometry. We extend this fast solver to non-rectangular geometries using the capacitance matrix method. We validate our solver on a vortex-shear instability test case in a circular domain, a vortex-wall interaction test-case, and on an idealized wind-driven double-gyre configuration in a octogonal domain at a eddy-permitting resolution. We release a concise, efficient, and auto-differentiable PyTorch implementation of our method to facilitate future developments upon this new discretization, *e.g.* machine learning parameterization or data-assimilation techniques.

1 Introduction

Ocean fluid dynamics offers a hierarchy of models that trade between richness of the physical phenomena and dimensionality of the system. On the one end of this hierachy are the Boussinesq non-hydrostatic equations. These equations describe the evolution of the stratification via temperature and ~~salinty~~salinity, they model explicitly convective phenomena but they require the evolution of six prognostic variables: the three components of the velocity $\mathbf{u}, \mathbf{v}, \mathbf{w}$, temperature $\mathbf{T}$ and salinity $\mathbf{s}$, and the free surface $\boldsymbol{\eta}$.

On the other end of this hierachy are the multi-layer quasi-geostrophic equations. These equations are based on strong hypotheses: static background stratification, hydrostatic and geostrophic balances. In a multi-layer QG model, the stream-function (SF) $\boldsymbol{\psi}$ and potential vorticity (PV) $\mathbf{q}$ are stacked in N isopycnal layers with density ρ_i and reference thickness

H_i:

$\boldsymbol{\psi} = [\psi_1, \dots, \psi_N]^T$,

$\mathbf{q} = [q_1, \dots, q_N]^T$.

The governing equations read

$$\partial_t \mathbf{q} + \begin{pmatrix} \mathbf{u} \\ \mathbf{v} \end{pmatrix} \cdot \nabla_{\mathrm{h}} \mathbf{q} = 0, \qquad \begin{pmatrix} \mathbf{u} \\ \mathbf{v} \end{pmatrix} = \nabla_{\mathrm{h}}^{\perp} \boldsymbol{\psi}, \tag{1a}$$

$$\Delta_{\mathrm{h}} \boldsymbol{\psi} - f_0^2 A \boldsymbol{\psi} = \mathbf{q} - \beta y, \tag{1b}$$

$$A = \begin{bmatrix} \frac{1}{H_1 g_0'} + \frac{1}{H_1 g_1'} & \frac{-1}{H_1 g_1'} & \cdot & \cdot \\ \frac{-1}{H_2 g_1'} & \frac{1}{H_2 g_1'} + \frac{1}{H_2 g_2'} & \frac{-1}{H_2 g_2'} & \cdot \\ \cdot & \cdots & \cdots & \cdots \\ \cdot & \cdot & \frac{-1}{H_n g_{n-1}'} & \frac{1}{H_n g_{n-1}'} \end{bmatrix}. \tag{1c}$$

$\nabla_{\mathrm{h}}^{\perp} = [-\partial_y, \partial_x]^T$ stands for the horizontal ~~perp-gradient~~orthogonal-gradient, $\Delta_{\mathrm{h}} = \partial_{xx}^2 + \partial_{yy}^2$ denotes the horizontal Laplacian. $f_0 + \beta(y - y_0)$ is the Coriolis parameter under beta-plane approximation with the meridional axis center y_0, $g_0' = g$ is the gravitational acceleration, and $g_i' = g(\rho_{i+1} - \rho_i)/\rho_i$ are the reduced gravities. One can include bottom topography as a constant term in the RHS of the QG elliptic equation (1b) (Hogg et al., 2014).

QG equations hence involve a single prognostic variable, the potential vorticity (PV) $\mathbf{q}$, which is advected (eq. 1a). Despite strong hypotheses, the multi-layer QG equations are a robust approximation of ocean meso-scale non-linear dynamics. They offer a computationally efficient playground to study the meso-scale ocean dynamics and to develop physical parametrizations of the unresolved eddy dynamics (Marshall et al., 2012; Fox-Kemper et al., 2014; Zanna et al., 2017; Ryzhov et al., 2020; Uchida et al., 2022, e.g.).

Solving the QG equations requires solving an elliptic equation (eq. 1b) which relates the streamfunction $\boldsymbol{\psi}$ and the potential vorticity $\mathbf{q}$. On a rectangular domain, it can be easily achieved using a fast spectral solver based on discrete Fourier transform (DFT) for periodic boundary conditions or discrete sine transform (DST) for no flow boundary conditions. Most of the available open-source QG solvers like Geophisical Flows (Constantinou et al., 2021), PyQG or Q-GCM (Hogg et al., 2014) use such spectral solvers and are therefore limited to rectangular geometries.

There are two major issues when implementing QG models on non-rectangular geometries. The first issue is the fact that spectral elliptic solvers do not apply for non-rectangular domains. In ocean models, one typically uses conjugate gradient (CG) iterative solvers like BiCGSTAB (Van der Vorst, 1992) to solve elliptic equations on non-rectangular domains, for example when solving the Poisson equations associated with a rigid lid-constraint (Häfner et al., 2021) or for implicit free-surface computations (Kevlahan and Lemarié, 2022) in Primitive equation solvers. These CG iterative solvers are significantly slower than spectral solvers to solve Poisson or Helmholtz equations on evenly spaced rectangular grids (Brown, 2020). Using them in a QG solver would reduce significantly the computational efficiency that makes QG appealing compared to Shallow-water (SW) models.

The second issue is the definition of the potential vorticity (PV) on the boundaries. If we discretize the potential vorticity $\mathbf{q}$ on the same locations as the streamfunction ψ, we have to define the potential vorticity on the boundaries. This requires using partial free-slip/no-slip condition (Hogg et al., 2014, see e.g.) to define ghost points in order to compute the laplacian of the streamfunction. ~~This ad-hoc definition might violate the global conservation of PV.~~

In this paper, we present `MQGeometry`, a new multi-layer QG equations solver that addresses these two issues. This solver uses a new discretization of the multi-layer QG equations based on two main ~~decisions~~choices. The first ~~decision~~ choice is to discretize the potential vorticity (PV) and the stream-function (SF) on two staggered grids. When doing so, the PV is not defined on the domain's boundary but in its interior. This solves the issue of defining the PV on the domain boundaries. Moreover, this ~~decision~~ choice allows using a finite-volume scheme for the PV advection. It ~~ensures~~ guarantees the global conservation of the PV and leverages a fine control on the PV fluxes. The second ~~decision~~ choice is to solve the elliptic equation using a fast spectral DST solver combined with the capacitance matrix method (Proskurowski and Widlund, 1976) to handle non-rectangular geometries.

In addition to this two ~~decisions~~choices, we decide to compute PV fluxes with upwind-biased stencil interpolation to remove the additional (hyper-)viscosity used in most discrete QG models. Doing so, we explore a different approach that is complementary to physical parameterizations of the horizontal momentum closure: a careful choice of the numerical schemes used to discretize the continuous equations. This idea has been initially developed by Boris et al. (1992) in the context of large eddy simulations (LES) models and made popular as implicit LES by Grinstein et al. (2007). It has been sucessfully tested by Von Hardenberg et al. (2000) to study vortex merging in single layer QG model and by Roullet et al. (2012) to study the forced-dissipated three dimensional QG turbulence in a channel configuration. While Von Hardenberg et al. (2000) and Roullet et al. (2012) used only linear upwind-biased recontruction, we implement here linear and non-linear weighted essentially non oscillatory (WENO) reconstructions (Jiang and Shu, 1996; Borges et al., 2008) that are tailored to remove spurious numerical oscillations created by linear reconstructions (Liu et al., 1994).

We implement the proposed discretizations in a concise Python-PyTorch code that allows seamless GPU acceleration. It benefits from built-in automatic differentiation to facilitate future developement in ~~machine-learing~~ machine-learning or data-assimilation. We validate our solver on a vortex-shear instability test case in a closed squared domain, an inviscid vortex-wall interaction, and an idealized wind-driven double-gyre configuration in a non-rectangular configuration.

This paper is organized as follows. In Section 2, we describe the resolution of the PV advection equation with finite volume. In Section 3, we present our elliptic solver based on discrete sine transform and capacitance matrix method (Proskurowski and Widlund, 1976). In Section 4, we detail the solver implementation. In Section 5, we describe the experimental settings to validate our discretization. We conclude and evoke further perspectives in Section 6.

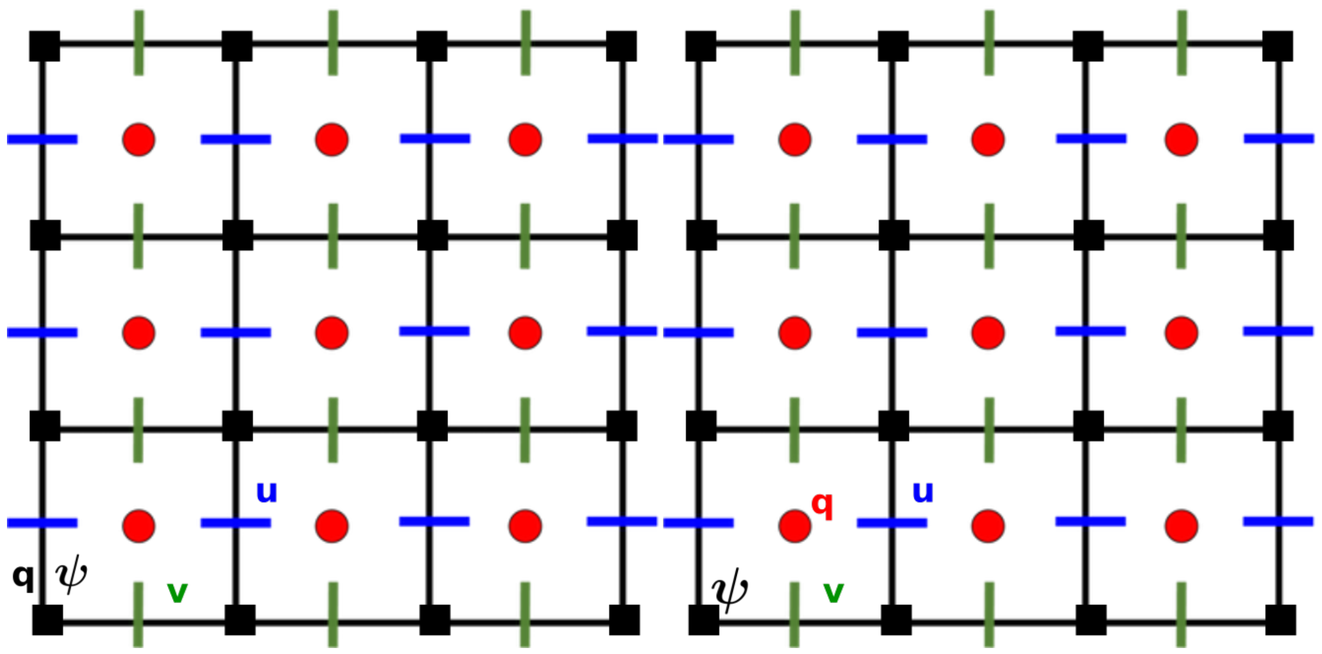

Figure 1. (left) usual and (right) proposed staggered discretization (bottom) of the prognostic variables ($\mathbf{q}$, ψ, $\mathbf{u}$, $\mathbf{v}$) for the QG system (1).

2 PV advection with finite volumes

2.1 Staggered discretization of PV and SF

The first ingredient of our method is to use finite-volumes to solve PV advection (eq. 1a). This leads ~~us~~ naturally to a staggered discretization for the PV and the SF (see right panel of Figure 1). With this choice, the PV advection (1a) can be integrated over the whole domain as a transported tracer with a finite volume formulation. Indeed, if ψ is discretized at the cell vertices, the ~~prep gradient~~ orthogonal-gradient of ψ computed with the standard second order discretization

$$\nabla_{\mathrm{h}}^{\perp} f_{i,j} = \begin{pmatrix} \frac{f_{i,j}-f_{i,j+1}}{\delta y} \\ \frac{f_{i+1,j}-f_{i,j}}{\delta x} \end{pmatrix}$$

~~lives~~ lies in the middle of the cell edges. The horizontal velocity $\mathbf{u}$ lives in the middle of the vertical egdes while the vertical velocity $\mathbf{v}$ lives in the middle of the vertical edges. We thus have to discretize the PV $\mathbf{q}$ at the cell centers to solve its advection with finite volumes.

At the boundary which passes along the cell edges, the condition is simply the no-flux of PV across the walls. This staggering clearly separates the boundary condition associated with the transport of PV from the boundary condition associated with ~~friction. Moreover, the~~ optional friction (partial free-slip or no-slip). The global conservation of PV during advection is ensured up to numerical precision with finite volumes.

In the usual discretization (see Appendix A), the PV must be defined on the boundary, which requires defining the Laplacian
95 operator Δ_h there. This is problematic since it forces blending the slip boundary conditions into the definition of the Laplacian, rather than having a slip boundary condition clearly separated from the definition of PV. Moreover, depending on this choice, the material conservation of the PV might not be ensured even though the advection scheme, *e.g.* Arakawa-Lamb (Arakawa and Lamb, 1981), conserves the PV inside ~~of~~ the domain.

2.2 Upwinding of PV fluxes

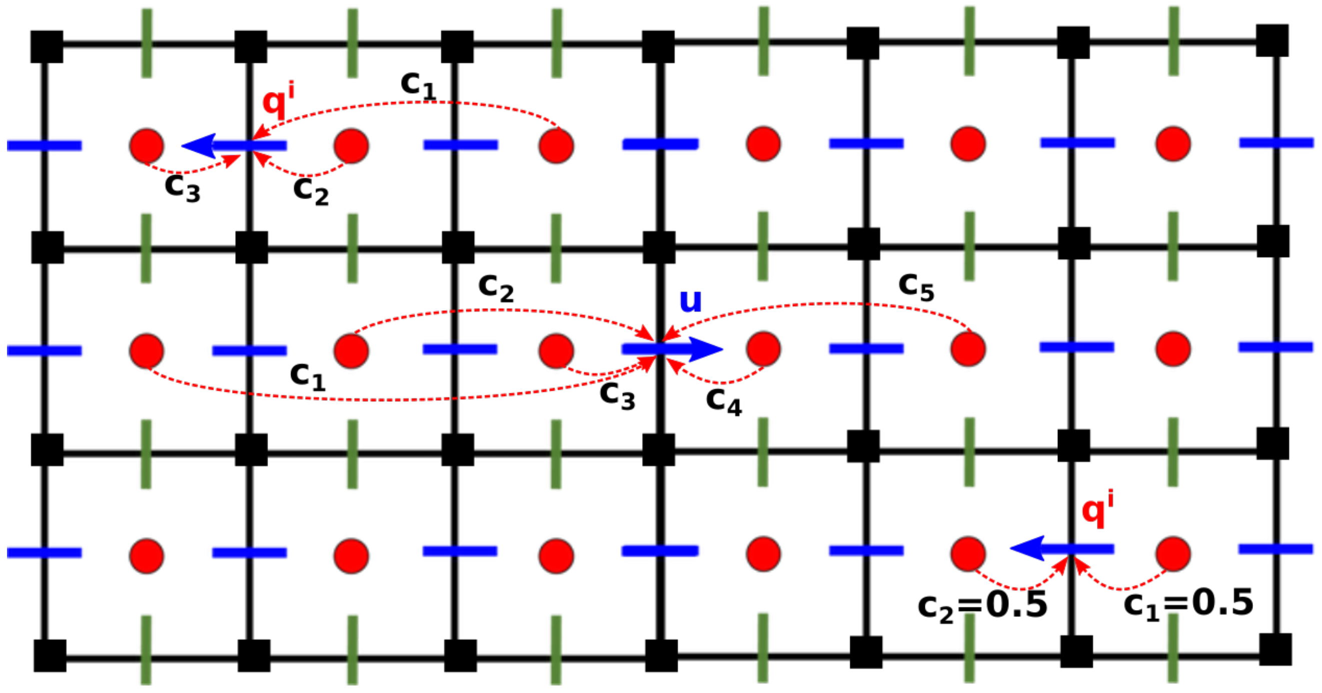

Figure 2. Illustration of the upwind biased reconstruction. Away from boundaries we use a 5-points stencil for reconstruction, while close to boundaries, we use a 3-points stencil when possible (top-left). At distance one from boundary when the velocity goes away from the boundary (bottom-right), we use a second order reconstruction with a two-points centered stencil rather than upwind-1 reconstruction to have a reconstruction of order at least two. For linear reconstructions, the weights c_i are fixed. For non-linear reconstruction, the weights c_i depend on the solution.

100 In a finite volume formulation, we rewrite the PV advection (1a) as the divergence of a flux:

$$\partial_t \mathbf{q} = -\nabla_\mathrm{h} \cdot \left(\begin{pmatrix} \mathbf{u} \\ \mathbf{v} \end{pmatrix} \mathbf{q} \right) . \tag{2}$$

The divergence is discretized with the usual second-order finite differences operator

$$\nabla_{\mathrm{h}} \cdot \begin{pmatrix} u_{i,j} \\ v_{i,j} \end{pmatrix} = \frac{u_{i+1,j} - u_{i,j}}{\delta x} + \frac{v_{i,j+1} - v_{i,j}}{\delta y}.$$

We hence need to interpolate $\mathbf{q}$ on the $\mathbf{u}$ and $\mathbf{v}$ grid points to compute these PV fluxes. In the context of finite volume methods, we call these interpolations *reconstructions*.

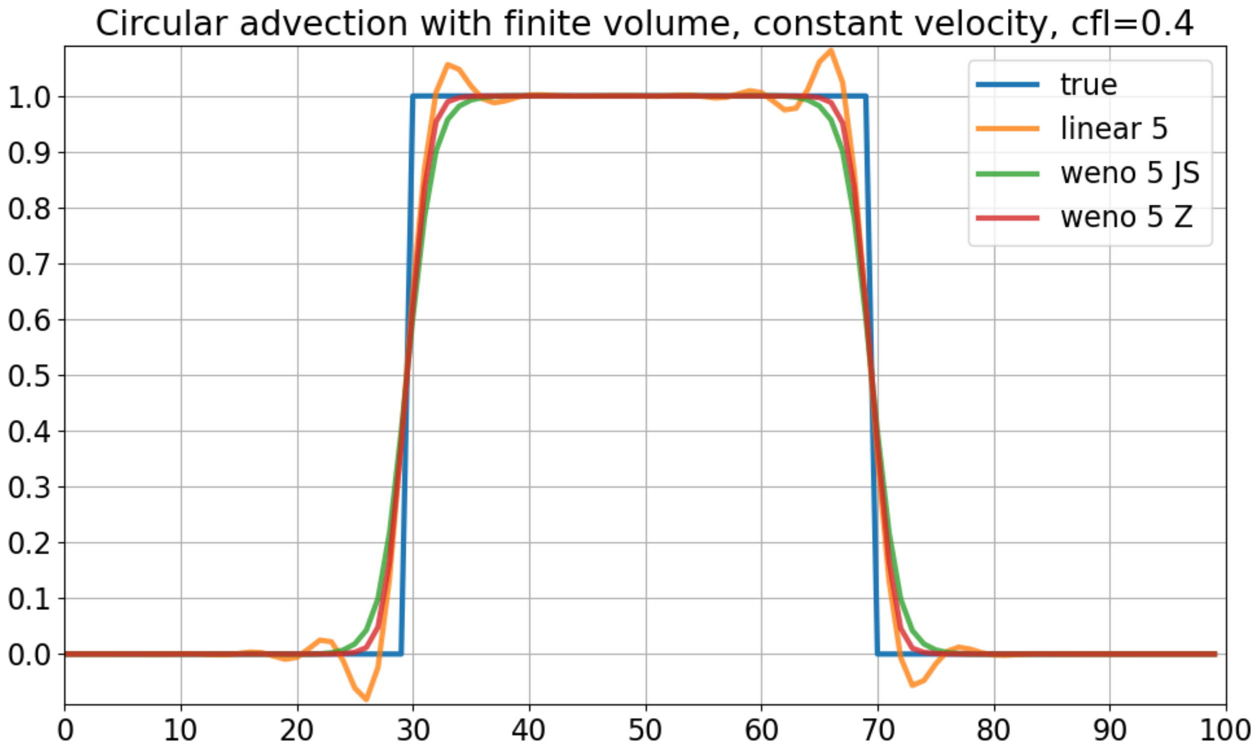

Figure 3. One dimensional advection with constant velocity on a periodic domain over one period. We compare 3 finite volume methods using linear, WENO-JS (Jiang and Shu, 1996), and WENO-Z (Borges et al., 2008) 5-points upwind reconstructions.

For a good trade-off between stability and accuracy, we use a 5-points upwind-biased stencil for reconstruction. Near the boundary we use a 3-points upwind-biased stencil or a 2-points centered stencil as illustrated in Figure 2. The ordering of the stencil is given by the sign of the velocity. For instance, $q^i = \sum_{s=1}^{5} c_s q_s$ when the velocity is positive, and we have the reverse order when the velocity is negative. Using upwind biased stencils for reconstruction allows removing additional ad-hoc (hyper-)viscosity which is necessary when using centered reconstructions (Lemarié et al., 2015). We decide here to rely solely on the upwinding to handle the potential enstrophy dissipation, which is done implicitely.

We offer two possibilities for reconstructions: linear reconstructions or Weighted Essentially Non Oscillatory (WENO) reconstructions (Liu et al., 1994). The weights c_s are fixed for the linear reconstruction. However, flux computed with linear reconstructions tend to produce spurious numerical oscillations when the field $\mathbf{q}$ is not smooth (see Figure 3).

WENO reconstructions benefit from the essentially non oscillatory property (Harten, 1984): they are designed to prevent spurious numerical oscillations that occur with linear reconstructions (see Figure 3). With a WENO scheme, the weights c_s are not fixed: they depend on the value of q on the five-point stencil via smoothness indicators, *e.g.* first and second-order deritatives computed with finite difference (Jiang and Shu, 1996). The smoother q on the stencil, the closer the weights c_s are to the linear weights. One can find a detailed explanation of these non-linear weights computations in Borges et al. (2008).

2.3 Time integration

WENO schemes' convergence and stability properties ~~of~~ derived in Jiang and Shu (1996) require using TVD Runge-Kutta scheme of order at least 3 (Shu and Osher, 1988). Here we use ~~Runge-Kutta TVD~~ TVD Runge-Kutta scheme of order 3 for time integration with finite time step δt.

Given the time ordinary differential equation

$$\partial_t f = Lf \ ,$$

one can write the ~~RK3 TVD~~ TVD RK3 scheme with the following three stages:

$$f^{(1)} = f^{(0)} + \delta t L f^{(0)} ,$$
$$f^{(2)} = f^{(1)} + \frac{\delta t}{4}\left(Lf^{(1)} - 3Lf^{(0)}\right) ,$$
$$f^{(3)} = f^{(2)} + \frac{\delta t}{12}\left(8Lf^{(2)} - Lf^{(1)} - Lf^{(0)}\right) .$$

This low memory version requires only the storage of the intermediate time derivatives $Lf^{(i)}$.

3 Spectral elliptic solver on non-rectangular domain

3.1 Staggering of PV and SF

After having solved PV advection equation (Eq. (1a)), one has to solve the elliptic equation (1b) to compute the SF. The SF ψ satisfies the homogeneous Dirichlet boundary condition, hence we have to compute the r.h.s. terms inside ~~of~~ the domain. Due to the staggered discretization, we need to interpolate them between the two grids. A natural way to proceed is to use a 4-points linear interpolation to interpolate $\mathbf{q}$ on the ψ-grid (see Figure 4).

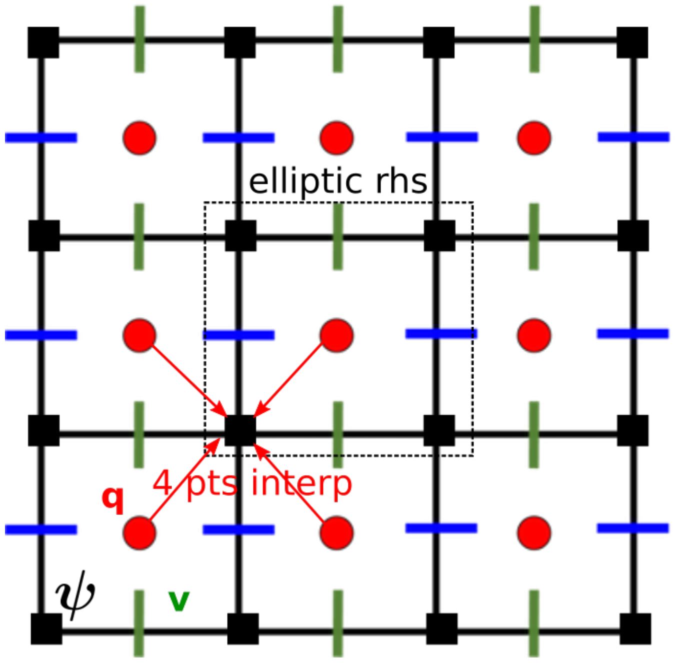

Figure 4. Illustation of the 4-pts interpolation to interpolate $\mathbf{q}$ on the $\boldsymbol{\psi}$-grid.

3.2 DST solver on rectangular geometry

To solve the elliptic equation (1b), we use a vertical transform and a fast spectral solver with discrete sine transform (DST). One can diagonalize the matrix A (defined in eq. 1c) as follows

140 $$A = C_{\mathrm{m2l}} \Lambda C_{\mathrm{l2m}} \ ,$$

where the layer-to-mode matrix C_{l2m} is the inverse of the mode-to-layer matrix C_{m2l}, and Λ is a diagonal matrix containing A eigenvalues. One can then perform the following layer-to-mode transform:

$$\widetilde{\boldsymbol{\psi}}, \, \widetilde{\mathbf{q}} = C_{\mathrm{l2m}} \boldsymbol{\psi}, \, C_{\mathrm{l2m}} \mathbf{q} \ .$$

With this transform, the elliptic equation (1b) becomes a stack of N two-dimensional Helmholtz equations

145 $$\Delta_{\mathrm{h}} \widetilde{\boldsymbol{\psi}} - f_0^2 \Lambda \widetilde{\boldsymbol{\psi}} = \widetilde{\mathbf{q}} - \beta y \tag{3}$$

with homogeneous Dirichlet boundary conditions. To solve these N two-dimensional Helmholtz equations, we use fast-diagonalization with type-I discrete sine transform (DST-I) since the usual 5-points Laplacian operator

$$\Delta_{\mathrm{h}} f_{i,j} = \frac{f_{i+1,j} - 2 f_{i,j} + f_{i-1,j}}{\delta x^2} + \frac{f_{i,j+1} - 2 f_{i,j} + f_{i,j+1}}{\delta y^2}$$

becomes a diagonal operator in the type-I sine basis (Press and Teukolsky, 2007, 20.4, p. 1055). After having solved these N Helmholtz equation, we transform back ψ from mode to layers

$$\psi = C_{\mathrm{m2l}} \widetilde{\psi} \, .$$

3.3 Capacitance matrix method for non-rectangular geometry

To handle non-rectangular domains, we use the capacitance matrix method (Proskurowski and Widlund, 1976). We have a non-rectangular domain $\Omega = \partial\Omega \cup \mathring{\Omega}$ where $\partial\Omega$ is the domain boundary and $\mathring{\Omega}$ is the interior of the domain. Our non-rectanglar domain Ω is embedded in a rectangular domain $\Omega_{\mathrm{R}} = \partial\Omega_{\mathrm{R}} \cup \mathring{\Omega}_{\mathrm{R}}$. ~~wW~~ We denote by $\mathcal{I} = \partial\Omega \setminus \partial\Omega_{\mathrm{R}}$ the set of ~~irregular~~ non-rectangular boundary indices (see Figure 5). We assume that we have K ~~irregular~~ non-rectangular boundary points $I_k \in \mathcal{I}$.

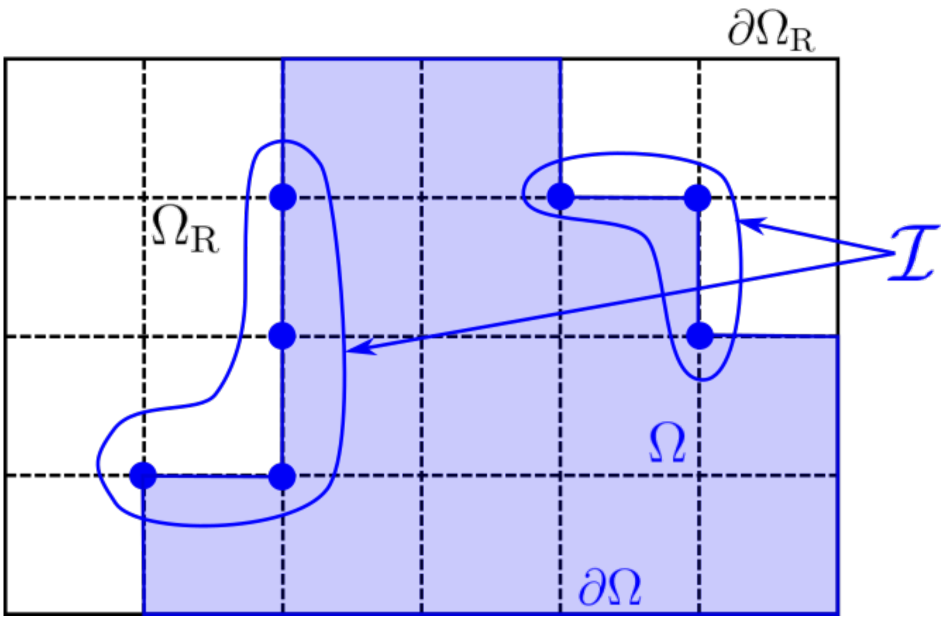

Figure 5. Domain Ω included in a rectangular domain Ω_{R}, and the set $\mathcal{I} = \partial\Omega \setminus \partial\Omega_{\mathrm{R}}$ of ~~irregular~~ non-rectangular boundary indices.

We now explain how to solve the following non-rectangular Helmholtz equation

$$\Delta_{\mathrm{h}} f - \lambda f = r \text{ in } \mathring{\Omega},\ \lambda \in \mathbb{R}^{+}, \quad f = 0 \text{ on } \partial\Omega \, . \tag{4}$$

One can find a more detailed explanation in Blayo and LeProvost (1993) as this is our inspiration for using the capacitance matrix method.

3.3.1 Pre-computations

For each ~~irregular~~ non-rectangular boundary point $I_k \in \mathcal{I}$, a Green function g_k ~~, we compute solutions~~ is defined as the solution of the following rectangular Helmholtz equation

$$\Delta_{\mathrm{h}} g_k - \lambda g_k = \begin{cases} 1 \text{ on } I_k \\ 0 \text{ in } \mathring{\Omega}_R \setminus \{I_k\} \end{cases} ,$$

$$g_k = 0 \text{ on } \partial\Omega_R \ .$$

solved using DST-I fast-diagonalization. With these Green functions, we compute the square matrix M with coefficients

$$m_{k,l} = g_l(I_k) \ .$$

We compute this matrix inverse to get the so-called capacitance matrix $C = M^{-1}$.

3.3.2 First-step

In a first step, we solve the following rectangular Helmhotz equation

$$\Delta_{\mathrm{h}} f^{(1)} - \lambda f^{(1)} = \begin{cases} r \text{ in } \mathring{\Omega} \\ 0 \text{ in } \mathring{\Omega}_R \setminus \mathring{\Omega} \end{cases}$$

$$f^{(1)} = 0 \text{ on } \partial\Omega_R$$

using DST-I fast-diagonalization. We then compute the vector s coefficients

$$s_k = f^{(1)}(I_k)$$

and we deduce the vector

$$\alpha = -Cs \ .$$

3.3.3 Second-step

In a second step, we solve the following rectangular Helmhotz equation

$$\Delta_{\mathrm{h}} f^{(2)} - \lambda f^{(2)} = \begin{cases} r \text{ in } \mathring{\Omega} \\ \alpha_k \text{ on } I_k \\ 0 \text{ in } \mathring{\Omega}_R \setminus \Omega \end{cases}$$

$$f^{(2)} = 0 \text{ on } \partial\Omega_R$$

using DST-I fast-diagonalization. This function $f^{(2)}$ is such that

$$\begin{aligned}\Delta_\mathrm{h} f^{(2)} - \lambda f^{(2)} &= r \text{ in } \mathring{\Omega}\\ f^{(2)}(I_k) &= 0 \;\forall I_k \in \mathcal{I}\\ f^{(2)} &= 0 \text{ on } \partial\Omega \setminus \mathcal{I}\end{aligned}$$

The restriction of $f^{(2)}$ over our non-rectangular domain Ω is therefore solution of the Helmholtz equation (4).

3.3.4 Numerical cost

The capacitance matrix method involves solving a dense linear problem with K unknowns, K being the number of boundary irregular points $\mathcal{I}$. The capacticance matrix is hence a $K \times K$ matrix, its inversions requires $\mathcal{O}(K^3)$ computations.

In practice, the inversion is the most computationnally expensive operation, but it is precomputed a single time. This methods' major limitation is in terms of memory, *i.e.* to store the $K \times K$ matrix especially on GPUs whose memory capacity is usually smaller than CPUs. On the laptop utilized, we were able to use up to $K = 10,000$, allowing us to run simulations akin to the North Atlantic at a resolution of 6km. At this resolution, the ageostrophic effects are becoming significant, and the QG hypothesis might no longer be relevant.

4 Implementation

4.1 Programming language and library

One can implement the above discretization using any programming language. To anticipate later applications in data assimilation and machine learning, and to benefit easily from GPU acceleration, we have decided to use the PyTorch library (Paszke et al., 2019). This library contains the usual linear algebra routines, and the computations can be easily vectorized. It offers a built-in automatic differentiation to compute gradients or adjoints~~, a feature that we do not use in the present study~~. This can be beneficial for future machine-learning and data-assimilation developments.

4.2 Upwind flux computation

Upwind flux computations require splitting the velocity into positive and negative part. This can be achieved very efficiently using the ReLU function

$$\mathrm{ReLU}(x) = \max(x, 0)$$

whose PyTorch implementation is highly optimized since this function is widely use in neural networks. The positive part u^+ and negative part u^- of the velocity are given by

$$u^+ = \mathrm{ReLU}(u),$$

$$u^- = u - u^+.$$

4.3 WENO reconstructions

Weighted essentially non-oscillatory (Liu et al., 1994, WENO) is a large class of reconstruction methods. We implement two of the most widely used WENO reconstructions: the WENO-JS (Jiang and Shu, 1996) and the WENO-Z (Borges et al., 2008). Implementating these methods require only a few lines of Python code (written in Appendix B).

4.4 Masks

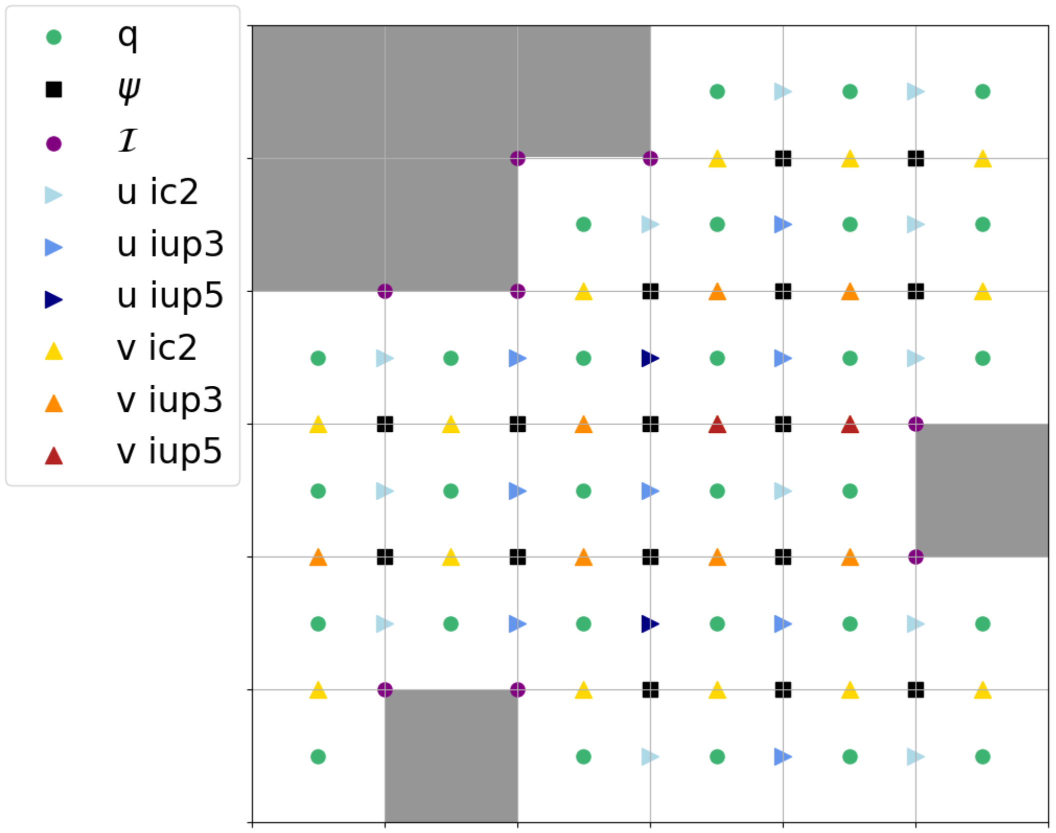

Figure 6. Illustration of the different masks. The label "u ic2" means that one uses two-points centered stencils to reconstruct $\mathbf{q}$ on these $\mathbf{u}$ points for PV fluxes computations. The label "v iup5" means that one uses five-points upwind-biased stencils to reconstruct $\mathbf{q}$ on these $\mathbf{v}$ points for vertical PV fluxes computations.

For non-rectangular domain, one has to provide a binary mask for the PV grid with ones inside the domain and zeros outside. Given this mask, we automatically compute the masks for the other variable, *i.e.* the stream-function ψ and the two components of the velocity $\mathbf{u}$ and $\mathbf{v}$, and we deduce the ~~irregular~~ non-rectangular boundary set $\mathcal{I}$ involved in the capacitance matrix computations. We also compute sepecific masks that specify the stencil for PV reconstruction on $\mathbf{u}$ and $\mathbf{v}$ points for PV fluxes computations. This is illustrated in Figure 6.

4.5 Elliptic solver

Our elliptic solver is based on fast diagonalization using discrete sine transform. Since PyTorch implements FFT but not DST, we implement DST-I using FFTs with specific pre- and post-processing operations. Notably, our DST-I implementation is faster than Scipy's implementation on Intel CPUs thanks to PyTorch bindings to MKL FFT.

The capacitance matrix method implementation is straightforward following the equations in section 3. Capacitance matrices are precomputed given the set of ~~irregular~~ non-rectangular boundary indices $\mathcal{I}$. The method solves the Helmholtz equation with machine precision accuracy. Figure 7 illustrates this point on a circular domain at resolution 256^2. From a prescribed streamfunction f, taken as Gaussian white noise and vanishing along the boundary, we apply the Helmholtz operator to get a r.h.s. We then solve the Helmholtz equation with this r.h.s. to get f_{inv}. Figure 7 shows that $f_{\text{inv}} - f$ is of the order of machine precision. The method is independant of the domain shape. The numerical experiments below explore various domain shapes.

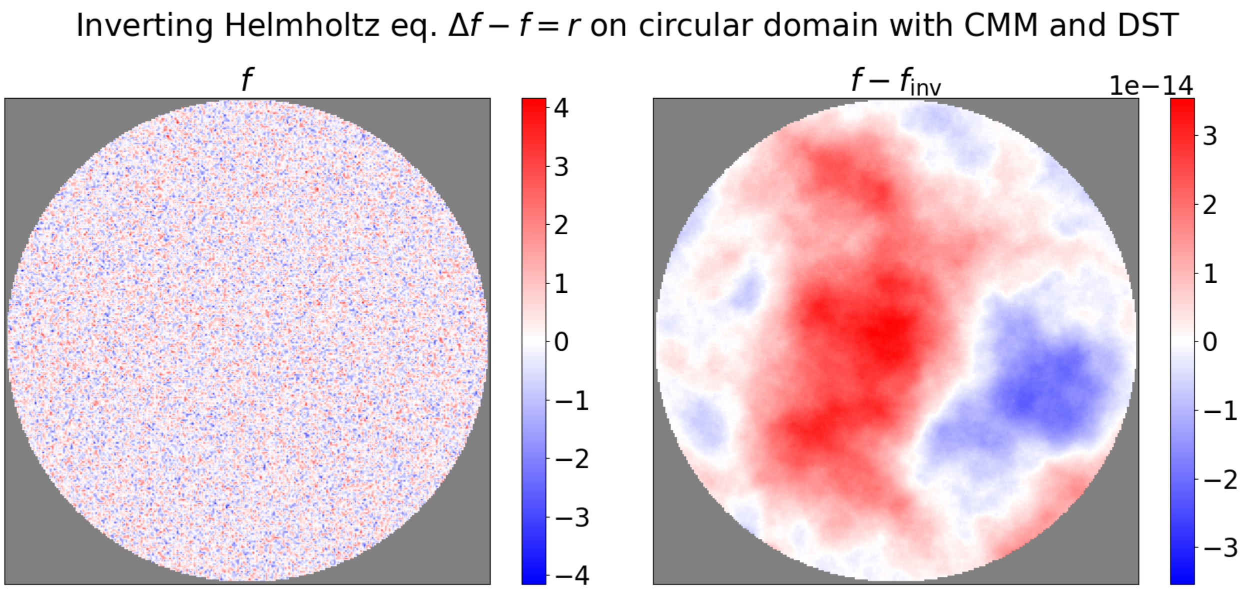

Figure 7. Example of Helmholtz equation solved with our solver on a circular domain embedded in a 256^2 square domain. The true function f is initialized with spatially uncorrelated Gaussian white noise. The inverted function f_{inv} is computed using our solver. The difference between f and f_{inv} is of the order of machine precision.

Our spectral solver can't handle curvilinear coordinates or non-constant metric terms. Solving the QG equations on a grid with non-constant metric requires an iterative elliptic solver, *e.g.* a multigrid solver (Fulton et al., 1986). Iterative solver can be speed-up with a good initial guess. One can still use the presented solver to provide an initial guess assuming that the metric terms dx and dy are constant, *e.g* equal to the mean dx and dy.

4.6 Compilation

PyTorch embeds a compiler which allows a significant speed-up for computationally intense routines. We compile the flux computations and finite difference routines. We get a 2.2× speed-up thanks to this compilation with `torch.compile`.

4.7 Ensemble simulations

Thanks to PyTorch vectorized operations, our implementation allows running ensemble simulations, *i.e.* parallel simulations starting from different initial conditions. This is a promising possibility for later developments of ensemble-based data assimilation or for stochastic extensions such as (Li et al., 2023).

4.8 Architecture

The code is divided into six python scripts:

- `helmholtz.py` which contains the Helmholtz solvers based on DST-I and capacitance matrix method.
- `fd.py` which contains the finite difference functions.
- `reconstruction.py` which contains the reconstructions (*i.e.* interpolations in the context of finite volumes) routines.
- `masks.py` which containts the mask utility module.
- `flux.py` which contains the flux computations routines.
- `qgm.py` which contains the python class implementing the multi-layer QG model.

We end up with a concise PyTorch implementation ($\sim$ 750 lines of code) which is as close as possible to the equations. It can run seamlessly on CPUs and GPUs with CUDA compatibility.

4.9 Performance

~~On~~

To assess the performance of our solver, we ran the double-gyre experiement (see below) on a Dell precision 7560 Laptop equipped with a Intel Core i9-11950H CPU and a NVIDIA RTX A3000 Laptop GPU. We measure the number of seconds per grid-point per time-step as well as the power comsumption of the devices using the commands `nvidia-smi` for GPU and `turbostat` for CPU.

Using the GPU, we get an execution time of ~~4.1×10^{-9}~~ 2.5×10^{-8} sec. per grid-point per ~~RK step on GPU (NVIDIA GeForce RTX 2080 Ti), and 4.8×10^{-8}~~ time-step with a power consumption of 75 Watt. Using the CPU with a single core, we get an execution time of 1.9×10^{-7} sec. per grid-point per ~~RK step on a single core CPU (Intel Core i9-11950H)~~time-step with a power consumption of 22 Watt. Using the full CPU with 16 cores, we get an execution time of 7.0×10^{-8} sec. per grid-point per time-step with a power consumption of 67 Watt.

As expected, the GPU has a better power efficiency than the CPU (Häfner et al., 2021). There is still room for improvement for CPU parallelization in our code, as PyTorch's native parallelism is not fully efficient in our case.

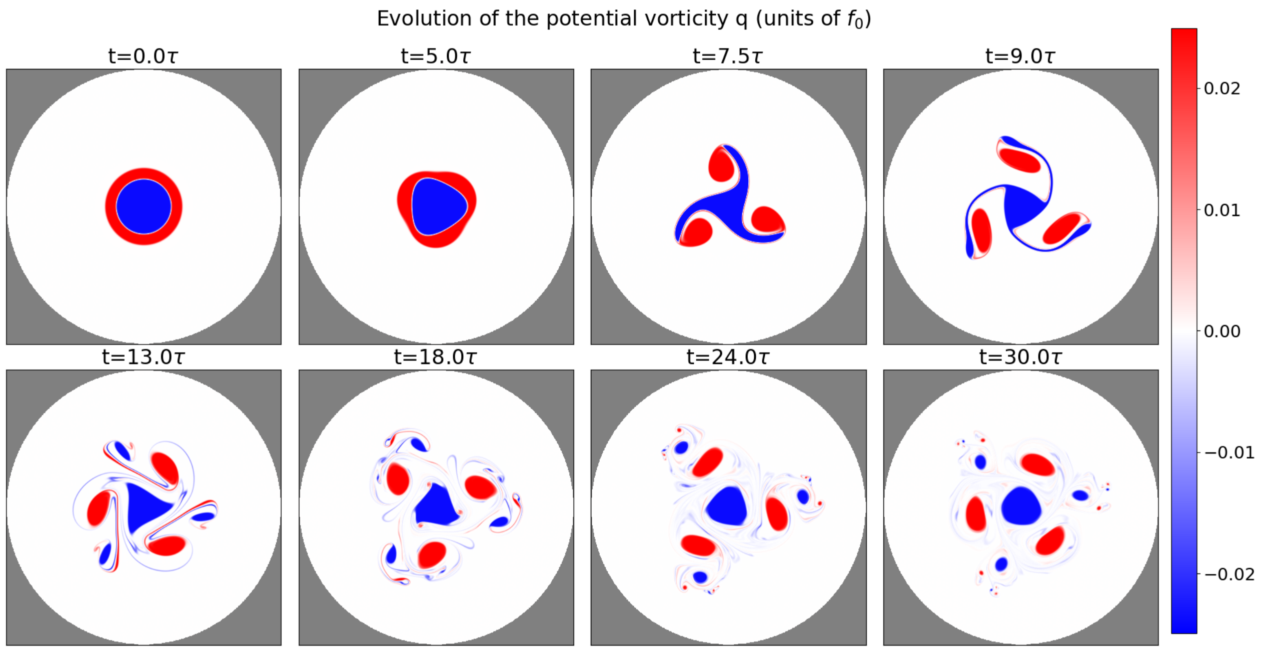

Figure 8. Vortex-shear instability experiement. Evolution of potential vorticity $\mathbf{q}$ at initial time $t = 0$, at intermediate times $5\tau, 7.5\tau, 9\tau, 13\tau, 18\tau, 24\tau$, and at final simulation time 30τ.

4.10 Accuracy

Despite the high-order WENO reconstruction used to solve the PV transport, our solver is formally second-order accurate due to the staggering and the use of second order perpendicular and divergence operator. This calls for a discussion.

The perpendicular gradient operator is applied to the stream function, which is the smoothest field that we resolve. The benefits of using higher-order schemes for this operator is less obvious. The second-order divergence operator used in finite-volume advection ensures the global conservation of PV up to numerical precision. Higher-order scheme might discard this conservation property. For the PV advection, low-order reconstruction schemes suffer from higher numerical diffusion (Lemarié et al., 2015) while linear reconstructions tend to create more oscillations for non-smooth fields. These two considerations motivate the use of high-order non-linear reconstruction on the potential vorticity field, which is non-smooth since QG flows contain boundary currents, eddies, and filaments.

5 Numerical validation

We run three numerical experiments involving meso-scale vortices (20 to 200 km diameters) to validate our solver. The first one is a vortex shear instability, the second one is a vortex wall interaction, and the third one is an idealized double-gyre experiement, which is a usual toy model for western boundary currents. ~~These experiments~~ With our solver, multi-layer QG equations deliver on their promise of computationally efficient playground to study meso-scale non-linear dynamics. Indeed, the three presented experiements ran on a laptop and took a few to to fifty minutes to run. We provide the python scripts to reproduce these experiments and the figures.

5.1 Vortex shear instability

The first validation of our method consists of a vortex shear instability. We consider a rotating fluid in a circular domain with diameter $D = 100\,\mathrm{km}$ embedded in a square domain of size $L_x \times L_y$ =100 km× 100km on a ~~f-plane~~ f-plane with a Coriolis parameter f_0, whose value is deduced below from the Burger number below. There is a single layer of fluid with reference thickness $H = 1\,\mathrm{km}$. We assume no-flow and free-slip boundary conditions. The gravity constant is set to $g = 10\,\mathrm{m\,s^{-2}}$.

We study the shear instability of a meso-scale shielded Rankine vortex, which has piece-wise constant potential vorticity. In the initial state, the vortex is composed of a core vortex surrounded by a ring of opposite-sign potential vorticity to the core such that the total sum of the PV is zero. This system is shear unstable and generates multipoles (Morel and Carton, 1994). We focus here on the tripole formation regime.

The core of the vortex has a radius $r_0 = 10\,\mathrm{km}$ and positive vorticity. The surrounding ring has an inner radius $r_0 = 10\,\mathrm{km}$ and $r_1 = 14\,\mathrm{km}$. The remaining parameters of the simulation are set via the Rossby and Burger numbers defined as follows

$$Ro = \frac{u_{\max}}{f_0 r_0}, \tag{5}$$

$$Bu = \frac{gH}{(f_0 r_0)^2}, \tag{6}$$

where $u_{\max}$ is the maximum velocity of the initial condition. Given the Burger number, we compute the Coriolis parameter using $f_0 = \sqrt{\frac{gH}{Bu\, r_0^2}}$. Then given the Rossby number, we rescale the velocity field of the initial condition such that the maximum velocity is $u_{\max} = Ro f_0 r_0$.

The quasi-geostrophic equations are valid for $Bu \leq 1$ and $Ro \ll 1$. We perform the experiment with $Ro = 0.01$ and $Bu = 1$. The ~~experiment is~~ equations are integrated over a period of $30\,\tau$, with $\tau = \|\mathbf{q}_{\mathrm{init}}\|_2^{-1}$ the eddy-turnover time, and $\mathbf{q}_{\mathrm{init}}$ the initial condition, shown at the top-left of Figure 8. At initial time the PV contours of the core and the ring $r = r_i$ are slightly perturbed by means of a mode three azymuthal perturbation defined in polar coordinates (r, θ) by

$$(1 + \epsilon \cos(3\theta))\, r = r_i\,,$$

where $\epsilon \ll 1$ is a small parameter, typically $\epsilon = 0.001$. This perturbation favors the growth of the most unstable mode which, given the ratio r_1/r_0, evolves nonlinearly into a tripole (Morel and Carton, 1994).

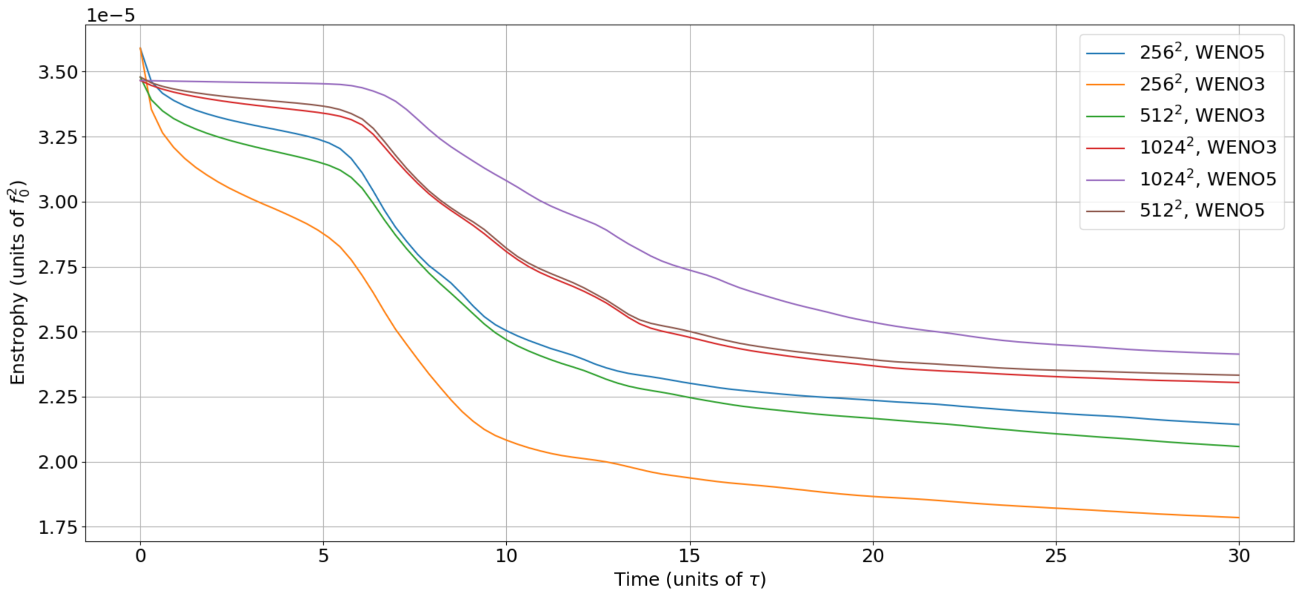

Figure 9. Evolution of the total enstrophy for the vortex-shear at resolutions 1024^2, 512^2, and 256^2 using WENO-3 or WENO-5 for PV reconstruction.

We use WENO-Z reconstructions for this experiment. This experiment can be reproduced with script `vortex_shear.py`. We run the reference experiment at a resolution of 1024^2.

We see on Figure 8 the evolution of the vortex potential vorticity $\mathbf{q}$ at different times between the beginning and the end of the simulation at time $t = 30\tau$. At time $t = 5\tau$ the result of the instability is visible and the core vortex which was initally circular has a ~~triagular~~ triangular shape. At time $t = 7.5\tau$ the outer positive PV ring has become the expected tripole (Morel and Carton, 1994). At time $t = 9\tau$ the core vortex recovers a triangular shape with negative PV filaments ranging from the triangle vertices to the three positive vortices. At time $t = 13\tau$, the core vortex keeps a triangular shape and the voriticity finalements are becoming thinner. At time $t = 18\tau$, the filaments thickness are reaching the grid scale and they start being dissipated by WENO-Z implicit dissipation. At time $t = 24\tau$, the filaments have are being progressively dissipated and have a smaller amplitude. The core vortex shape is become more circular, and the three positive vortices are surrounded by a smaller negative vortex. At final time $t = 30\tau$, the filaments amplitude have lowered, and small vorticity dipoles appear. The order three symmetry, that was injected by the initial perturbation, starts to be lost only at time $t = 30\tau$. For later times (not shown), the system evolves into a chaotic system. This chaotic evolution is expected as the system is sensitive to initial conditions.

To measure the sensitivity of our solver to resolution ~~, we consider the~~ and to order of the reconstruction scheme (3 or 5), we compare the solutions produced by our solver at resolution 1024^2~~resolution as the high resolution reference, and we run the simulation at two lower resolutions:~~ , 512^2, and 256^2 ~~, and 512^2. At the top of~~ using third-order WENO (WENO-3) and fifth-order WENO (WENO-5) reconstructions. In Figure 9 we plot the evolution of the total enstrophy at the three different resolutions. The results show that the enstrophy dissipation decreases as the resolution increases, indicating that a higher resolution better preserves the PV variance, and that low resolution simulations suffer from an excessive dissipation.

We also note that WENO-3 leads to excessive numerical dissipation compared to WENO-5. Moreover, the enstrophy is better preserved with WENO-5 at resolution 512^2 than with WENO-3 at resolution 1024^2. We plot on Figure C1 in appendix the final state of the simulation at resolutions 512^2 and 1024^2 with WENO-3 and WENO-5. This indicates that WENO-5 increases the effective resolution. In terms of computation cost, the simulation runtime is 1 minute 2 secondswith WENO-5 at resolution 512^2 and 5 minutes 52 seconds WENO-3 at resolution 1024^2 with the NVIDIA RTX A3000 Laptop GPU. This illustrates the benefits of using high-order reconstructions despite the fact that our code is globally second-order accurate.

5.2 Vortex-wall interaction

To challenge the numerics we now study the propagation of a single meso-scale vortex along a solid boundary, with a free slip boundary condition. The domain is square with a thin wall obstacle. Because the flow is inviscid, up to numerical errors, the vortex is expected to follow the boundary according to the mirror effect. In particular the vortex should slip around the obstacle and litteraly circumvent it, without detaching from it, without producing filaments (Deremble et al., 2016). The challenge is thus to have a solution as inviscid as possible, and to enforce as better as possible both the no-flow and the free-slip boundary conditions.

The setup is as follows. The domain size is $L_x \times L_y = 100\,\mathrm{km} \times 100\,\mathrm{km}$ on a ~~f-plane~~ f-plane with a Coriolis parameter f_0. The thin wall obstacle is vertical starting from the middle of the domain south boundary and of length $L_y/4$ (see Figure 10) and has a two cells width. There is a single layer of fluid with reference thickness $H = 1\,\mathrm{km}$. We assume no-flow and free-slip boundary conditions. The gravity constant is set to $g = 10\,\mathrm{m\,s^{-2}}$. In the initial state, the vortex is a circle of radius $r_0 = 10\,\mathrm{km}$ with constant potential vorticity and is at the bottom of the domain and at the left of the wall. The circular shape differs from the oval shape a vortex has when moving along a rectilinear wall. The remaining parameters of the simulation are set via the Rossby and Burger with $Ro = 0.01$, and $Bu = 1$

Figure 10 shows PV snapshots at various times, superimposed with the streamfunction. The vortex behaves according to the inviscid regime. It clearly follows the wall and the obstacle elastically, without any sign of dissipative process such as filament detachement. The vortex at $t = 22\,\tau$ has recovered the characteristic oval shape. Between $t = 9.4\,\tau$ and $t = 12.6\,\tau$ the vortex circumvents the edge which causes it to experience its maximal deformation, but the solution remains ~~very~~ smooth. The streamfunction is clearly constant along the boundary, as a direct consequence of the capacitance matrix method. During the circumvention, it remains so, despite the thin wall imposing a strong curvature at the edge.

This experiment shows that the numerics has very good conservation properties on inviscid flows. This may come as a surprise since the upwinding does induce a numerical dissipation. In practice, the dissipation seems to self adjust to the minimum required to prevent noise at the grid scale. This way of discretizing, in line with the ILES approach, turns out to be a viable alternative to conservative discretization combined with an explicit dissipation term.

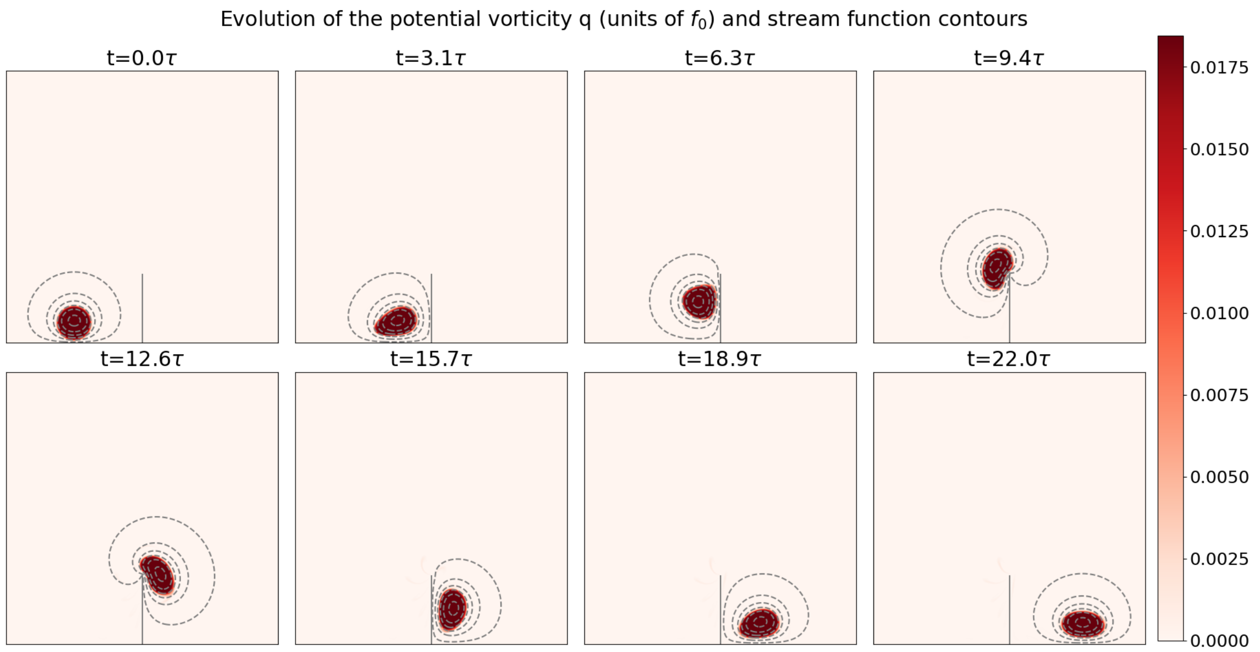

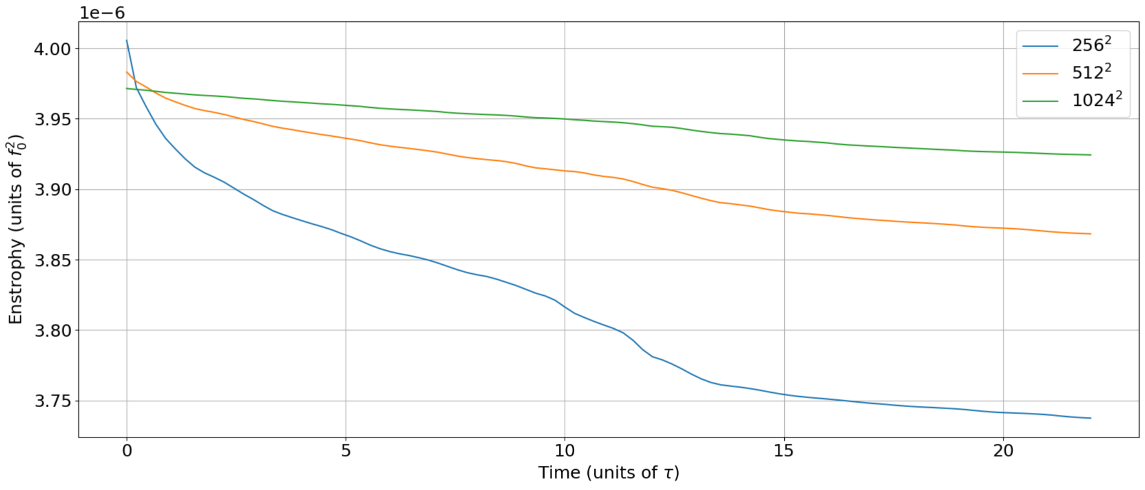

Figure 10. Vortex-wall interaction experiement. (Top) Vortex potential vorticity $\mathbf{q}$ and streamfunction ψ contours at initial time $t = 0$, at intermediate times $3.1\tau, 6.3\tau, 9.4\tau, 12.6\tau, 15.7\tau, 18.9\tau$, and at final simulation time 22τ. (Bottom) Evolution of the total enstrophy at resolutions 1024^2, 512^2, and 256^2.

At the bottom of Figure 10 we plot the evolution of the total enstrophy at the three different resolutions. Once again, we note that the enstrophy dissipation decreases as the resolution increases: higher resolutions better preserve the PV variance, while low resolution simulations suffer from more dissipation.

Table 1. Parameters of the idealized double-gyre configuration

Parameters	Value	Description
$L_x \times L_y$	(5120×5120) km	Domain size
$n_x \times n_y$	256×256	Grid dimension
dx $\times$ dy	20$\times$20 km	Spatial resolution
H_k	$(400, 1100, 2600)$ m	Layer thickness
g'_k	$(0.025, 0.0125)$ m s^{-2}	Reduced gravity
δ	$1.43\,10^{-5}$ s^{-1}	Bottom drag coef.
τ_0	0.08 N m^{-2}	Wind stress magnitude
ρ_0	1000 kg m^{-3}	Ocean density
f_0	$9.375\,10^{-5}$ s^{-1}	Mean Coriolis
β	$1.754\,10^{-11}$ (m s)$^{-1}$	Coriolis gradient
L_d	$(41, 25)$ km	Rossby radii
dt	4000 s	Time-step

5.3 Double-gyre configuration

Our ~~second~~ third numerical experiment to validate our solver is an idealized double-gyre configuration. Double-gyre ~~configuration~~ configurations are a natural test for QG implementation or parameterization (Zanna et al., 2017; Ryzhov et al., 2020; Uchida et al., 2022, e.g.). We consider here an octogonal ocean basin to illustrate the ability of our solver to handle non-square geometries. This octogon has maximal dimensions $L_x \times L_y$. We assume free-slip boundary conditions on the boundaries. We consider $N = 3$ layers on the vertical. We use an idealized stationary and symmetric wind stress (τ_x, τ_y) with $\tau_x = -(\tau_0/\rho_0)\cos(2\pi y/L_y)$ and $\tau_y = 0$ on the top and linear drag at the bottom drag coefficient δ. The parameter values are given in Table 1.

We study this configuration in an eddy-permitting resolution of 20km the eddy-resolving meaning that the spatial resolution (20km) is half of the larger baroclinic Rossby radius (41km). ~~At~~ Already at such eddy-permitting resolution, multi-layer QG solvers do not necessarily produce a well-pronounced eastward jet and usually require additional eddy parameterization (Uchida et al., 2022).

We plot on top of Figure 11 a snapshot of upper-layer streamfunction and relative vorticity (*i.e.* $\Delta\psi$) after 30 years of spin-up. As expected, our solver produces a strong western boundary current on the vertical and non-vertical boundaries. In the middle of this boundary starts a well extended eastward jet whose length is qualitatively comparable with the Gulf-stream length in the North-Atlantinc basin. This jet is surrounded by a recirculation zone ~~in which are~~ with several meso-scale eddies~~.~~ , which appears coherent with eddy-resolving resolution simulations. We notice large scale Rossby waves that are emerging near the eastern boundary and that propagate westward.

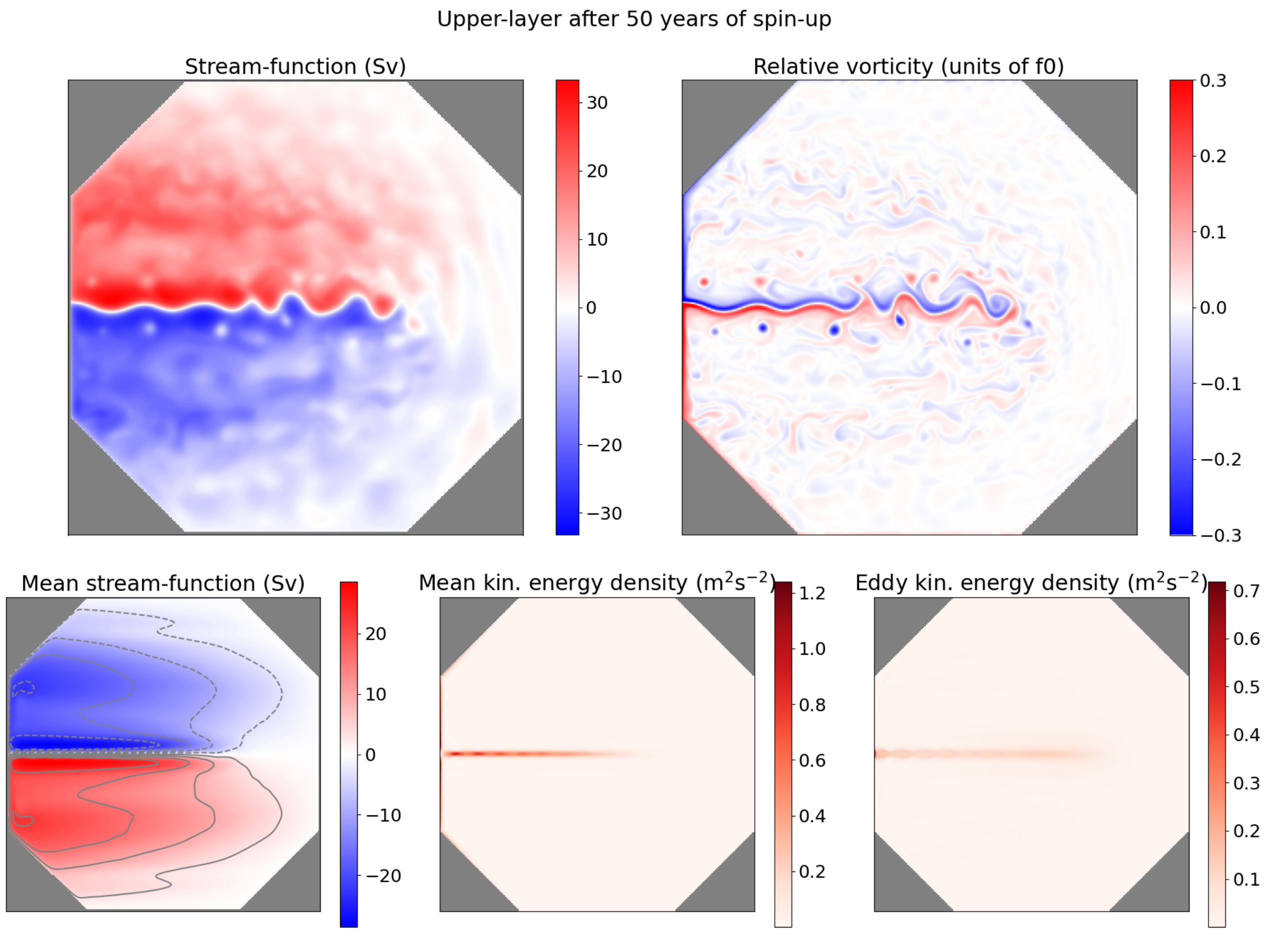

Figure 11. (Top) Upper-layer stream function ψ and relative vorticity (*i.e.* $\Delta\psi$) after 50 years of spin-up. (Bottom) Upper-layer mean stream function, mean kinetic energy density, and eddy kinetic energy density computed over 40 years after 10 years of spin-up.

Since this system is ~~cahotic~~chaotic, showing a snapshot is not very representative of the dynamical behaviour of the system. We plot statistics of our solution on ~~Bottom~~ the bottom of Figure 11: the mean stream-function, the mean kinetic energy (*i.e.* the kinetic energy of the mean velocity), and the eddy kinetic energy (*i.e.* the kinetic energy of the velocity standard deviation). These statistics were computed over 40 years after 10 years spin-up, saving one snapshot every 15 years. These statistics are symmetric which is expected since the domain shape and the wind forcing are symetric. They confirm the presence of a strong western boundary currents and fluctuating eastward jet whose length is roughly three fourth of the domain. These results seem to confirm the relevance of implicit dissipation provided by upwinding, since usual multi-layer QG solvers require ~~require~~ additional eddy parameterization (Uchida et al., 2022) to produce a well-pronounced eastward jet.

To assess the influence of the resolution on the solution produced by our solver, we run the same double-gyre experiment at lower resolutions: 27km, 40km, and 53km. We plot the the mean stream-function, the mean and eddy kinetic energy statistics

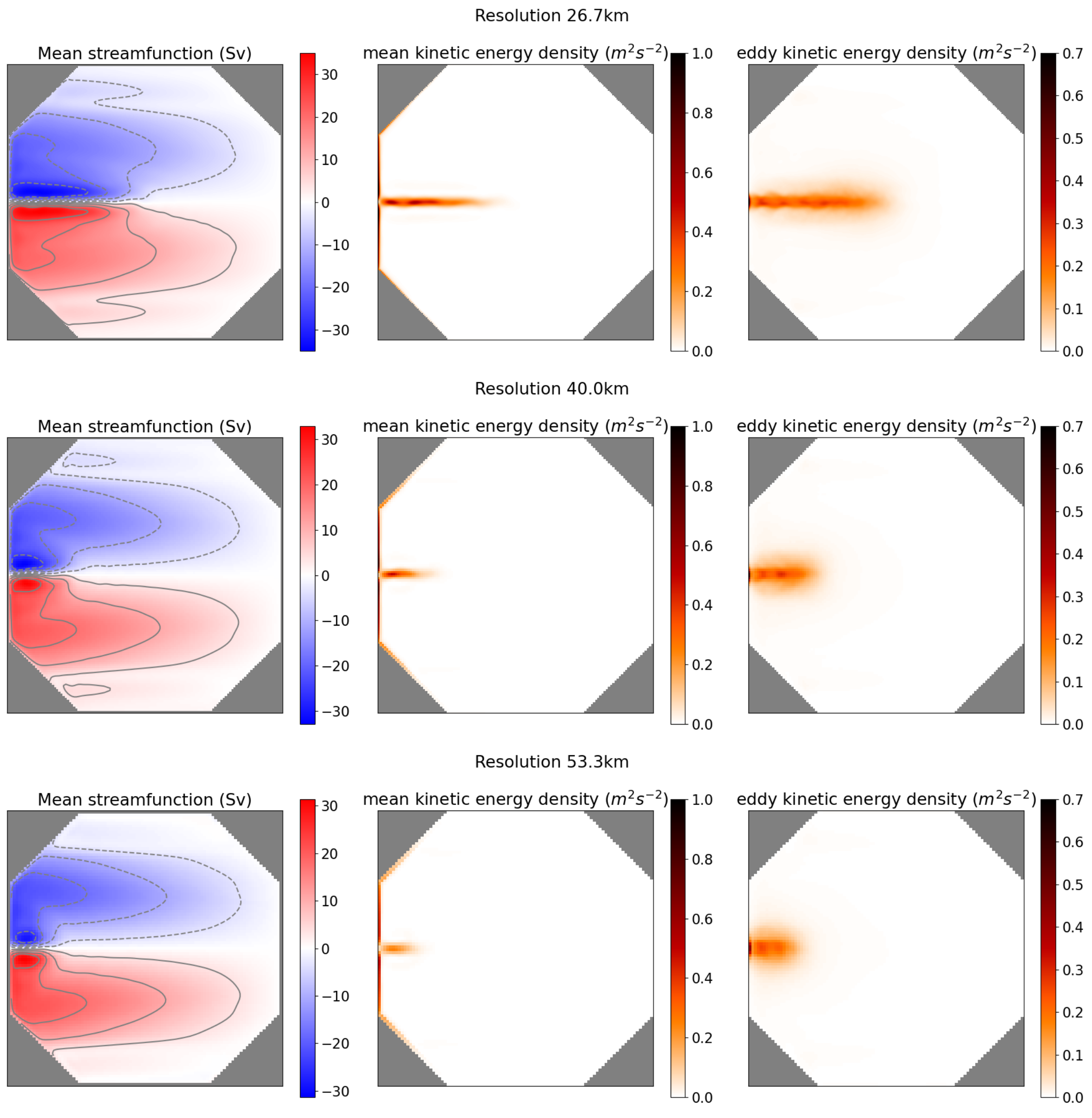

Figure 12. Upper-layer mean stream function, mean kinetic energy density, and eddy kinetic energy density computed over 40 years after 10 years of spin-up at resolutions (top to bottom) 27km, 40km, and 53km.

on Figure 12. We note that the eastward jet progressively diminishes as the resolution decreases: at resolution 27km, it bearly reaches the middle of the domain, while at resolutions 40km and 53km, it almost disappears. At these two coarsest resolutions that are comparable to the largest baroclinic Rossby radius, 41km in our configuration, meso-scale eddies can not be resolved properly by our solver, one would require an additional eddy parametrisation to produce the eastward jet (Zanna et al., 2017).

6 Conclusions

We presented `MQGeometry`, a multi-layer quasi-geostrophic equations solver for non-rectangular geometries. This solver has three original aspects compared to usual solvers like Q-GCM, PyQG or PEQUOD: the use of finite-volume for advection via staggering of the potential voriticity and stream-function, the non-linear WENO upwind-biased reconstructions with implicit dissipation, and the ability to handle non-square geometry with a fast spectral DST solver combined with the capacitance matrix method. Running a simulation with this solver does not require the tuning of any additional parameter, *e.g.* additional hyper-viscosity.

This multi-layer QG solver delivers a computationally efficient playground to study meso-scale non-linear dynamics. It opens the path to study the QG dynamics in basin with realistic coast line, *e.g.* ~~Mediterranea~~ Mediterranean or North-Atlantic basins. Moreover, with PyTorch automatic differentiation, one can easilly build upon this implementation to develop new machine learning parameterizations of the QG sub-grid scales or new data-assimilation techniques using QG.

We believe that more complex modeling systems can be implemented in high-level languages like Python without sacrifying performance as demonstrated by Häfner et al. (2021). The QG system that we implemented in this solver is fairly simple, and the present solver shall be seen a proof of concept. Our plan is to extend the presented approach to shallow-water equations and subsequently to primitive equations. Major advantages are the seamless parallelism offered by GPUs, enabling us to write code that closely aligns with the continuous equations, and the automatic differentiation, allowing to learn vertical parameterization in a end-to-end fashion (Kochkov et al., 2023).

Code availability. The python source code to reproduce the results is accessible on line at https://github.com/louity/MQGeometry. It contains a readme file with the instructions to run the code and a script to compute statistics and reproduce the figures.

Appendix A: Usual discretization of multi-layer QG equations.

One typically solves multi-layer QG equations using the following strategy (Hogg et al., 2014, e.g.) :

1. Use an evenly spaced Arakawa C-grid with the PV and the SF discretized on the same location, namely the cell vertices (see left panel of Figure 1).

2. Solve the PV advection equation (1a) using energy-enstrophy conservative Arakawa-Lamb scheme (Arakawa and Lamb, 1981) in the interior domain (*i.e.* not on the boundaries).

3. Since the scheme is energy conserving, use an additional (hyper-)viscosity scheme to dissipate the energy fueled by the wind forcing.

4. Given the matrix A diagonalization

   $$A = C_{\mathrm{m2l}} \Lambda C_{\mathrm{l2m}} \ ,$$

   where the layer-to-mode matrix C_{l2m} is the inverse of the mode-to-layer matrix C_{m2l}, and Λ is a diagonal matrix containing A eigenvalues, perform the following layer-to-mode transform:

   $$\widetilde{\boldsymbol{\psi}},\ \widetilde{\mathbf{q}} = C_{\mathrm{l2m}}\boldsymbol{\psi},\ C_{\mathrm{l2m}}\mathbf{q} \ .$$

   With this transform, the elliptic equation (1b) becomes a stack of N two-dimensional Helmholtz equations

   $$\Delta_{\mathrm{h}}\widetilde{\boldsymbol{\psi}} - f_0^2 \Lambda \widetilde{\boldsymbol{\psi}} = \widetilde{\mathbf{q}} - \beta y \tag{A1}$$

   with homogeneous Dirichlet boundary conditions.

5. Solve these N two-dimensional Helmholtz equations, using *e.g.* fast-diagonalization with type-I discrete sine transform (DST-I):

   $$\text{DST-I}[x]_k = \sum_{l=1}^{L} x_l \sin\left[\frac{\pi l k}{L+1}\right],\ k = 1 \ldots L \ .$$

6. Transform back from mode to layers

   $$\boldsymbol{\psi},\ \mathbf{q} = C_{\mathrm{m2l}}\widetilde{\boldsymbol{\psi}},\ C_{\mathrm{m2l}}\widetilde{\mathbf{q}} \ .$$

7. Update the PV boundary values using the elliptic equation (1b). This requires defining the Laplacian on the boundaries and possibly involves partial free-slip/no-slip boundary condition.

Appendix B: WENO implementation

```
def weno5(qmm, qm, q0, qp, qpp):
    """ WENO Jiang Shu 1996."""
    eps = 1e-8
    qi1 = 1/3*qmm - 7/6*qm + 11/6*q0
    qi2 = -1/6*qm + 5/6*q0 + 1/3*qp
    qi3 = 1/3*q0 + 5/6*qp - 1/6*qpp

    k1, k2 = 13/12, 0.25
    beta1 = k1 * (qmm-2*qm+q0)**2\
          + k2 * (qmm-4*qm+3*q0)**2
    beta2 = k1 * (qm-2*q0+qp)**2\
          + k2 * (qm-qp)**2
    beta3 = k1 * (q0-2*qp+qpp)**2\
          + k2 * (3*q0-4*qp+qpp)**2

    g1, g2, g3 = 0.1, 0.6, 0.3
    w1 = g1 / (beta1+eps)**2
    w2 = g2 / (beta2+eps)**2
    w3 = g3 / (beta3+eps)**2

    qi_weno5 = (w1*qi1+w2*qi2+w3*qi3)\
                / (w1+w2+w3)

    return qi_weno5

def weno5z(qmm, qm, q0, qp, qpp):
    """ WENO-Z Borges et al. 2008"""
    eps = 1e-14
    qi1 = 1/3*qmm - 7/6*qm + 11/6*q0
    qi2 = -1/6*qm + 5/6*q0 + 1/3*qp
    qi3 = 1/3*q0 + 5/6*qp - 1/6*qpp

    k1, k2 = 13/12, 0.25
    beta1 = k1 * (qmm-2*qm+q0)**2\
          + k2 * (qmm-4*qm+3*q0)**2
    beta2 = k1 * (qm-2*q0+qp)**2\
          + k2 * (qm-qp)**2
    beta3 = k1 * (q0-2*qp+qpp)**2\
          + k2 * (3*q0-4*qp+qpp)**2

    tau = torch.abs(beta1 - beta3)
    g1, g2, g3 = 0.1, 0.6, 0.3
    w1 = g1 * (1 + tau/(beta1+eps))
    w2 = g2 * (1 + tau/(beta2+eps))
    w3 = g3 * (1 + tau/(beta3+eps))

    qi_weno5 = (w1*qi1+w2*qi2+w3*qi3)\
               / (w1+w2+w3)

    return qi_weno5
```

Appendix C: Vortex shear instability

Author contributions. L.T. implemented the Pytorch software, conducted the numerical experiements, and wrote the article. G.R. gave the original idea of the staggering and the use of WENO, supervised the numerical experiments, and corrected the paper. L.L. helped with numerical experiements. E.M. supervised the project.

Competing interests. The authors declare no competing interests.

Acknowledgements. The authors acknowledge the support of the ERC EU project 856408-STUOD. We would like to express our warm thanks to Laurent Debreu for pointing us to the capacitance matrix method. We also thank Nicolas Crouseilles, Pierre Navaro, Erwan Faou, and Georges-Henri Cottet for the amicable exchanges and interesting discussions.

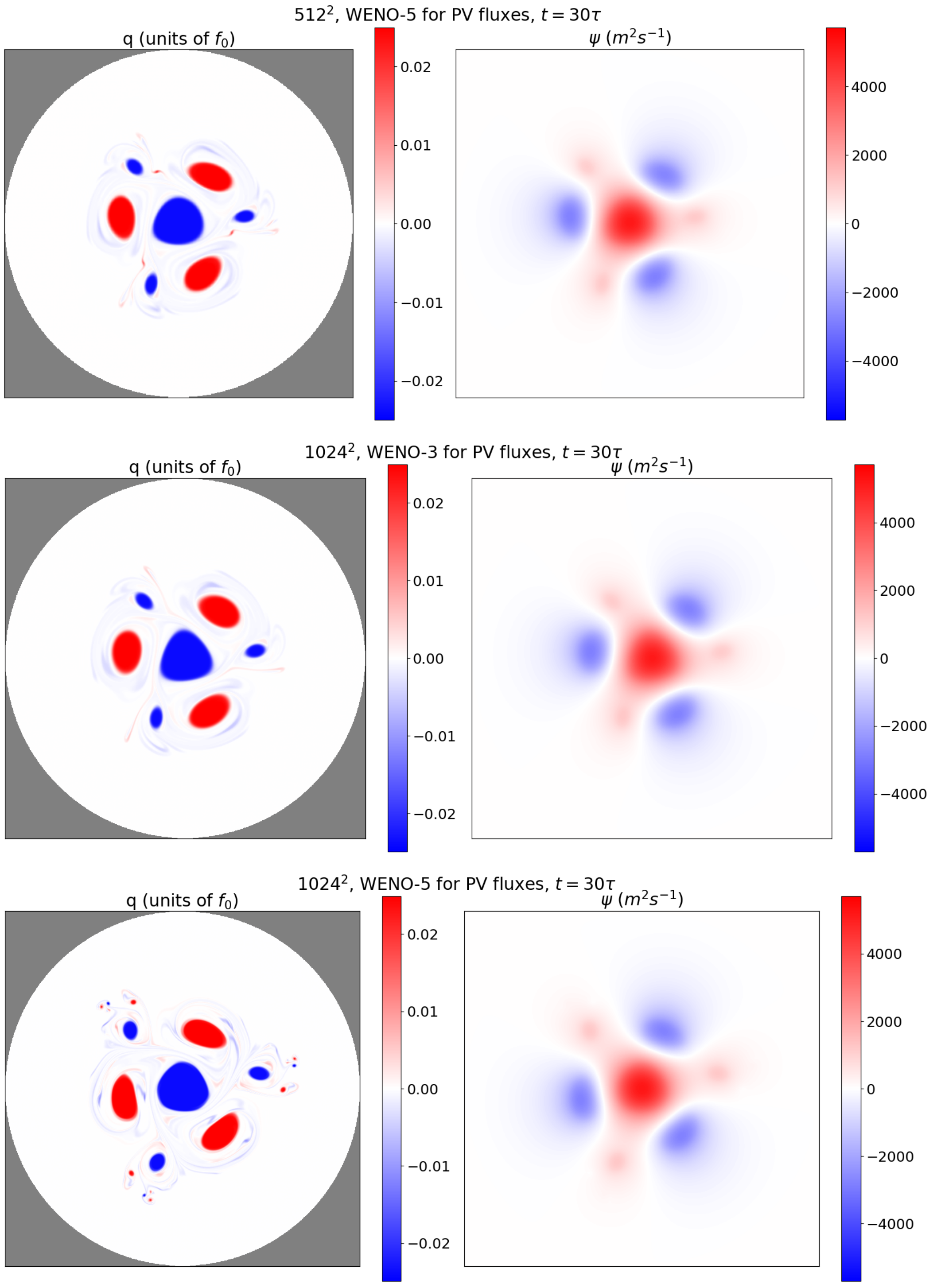

Figure C1. Vortex shear instability final-state ($t = 30\tau$) with resolution 512^2 and WENO-5 and with resolution 1024^2 and WENO-3/WENO-5.

References

Arakawa, A. and Lamb, V. R.: A potential enstrophy and energy conserving scheme for the shallow water equations, Monthly Weather Review, 109, 18–36, 1981.

Blayo, E. and LeProvost, C.: Performance of the Capacitance Matrix Method for Solving Helmhotz-Type Equations in Ocean Modelling, Journal of Computational Physics, 104, 347–360, 1993.

Borges, R., Carmona, M., Costa, B., and Don, W. S.: An improved weighted essentially non-oscillatory scheme for hyperbolic conservation laws, Journal of Computational Physics, 227, 3191–3211, 2008.

Boris, J. P., Grinstein, F. F., Oran, E. S., and Kolbe, R. L.: New insights into large eddy simulation, Fluid dynamics research, 10, 199, 1992.

Brown, N.: A comparison of techniques for solving the Poisson equation in CFD, arXiv preprint arXiv:2010.14132, 2020.

Constantinou, N. C., Wagner, G. L., Siegelman, L., Pearson, B. C., and Palóczy, A.: GeophysicalFlows.jl: Solvers for geophysical fluid dynamics problems in periodic domains on CPUs & GPUs, Journal of Open Source Software, 6, 3053, https://doi.org/10.21105/joss.03053, 2021.

Deremble, B., Dewar, W. K., and Chassignet, E. P.: Vorticity dynamics near sharp topographic features, Journal of Marine Research, 74, 249–276, 2016.

Fox-Kemper, B., Bachman, S., Pearson, B., and Reckinger, S.: Principles and advances in subgrid modelling for eddy-rich simulations, Clivar Exchanges, 19, 42–46, 2014.

Fulton, S. R., Ciesielski, P. E., and Schubert, W. H.: Multigrid methods for elliptic problems: A review, Monthly Weather Review, 114, 943–959, 1986.

Grinstein, F. F., Margolin, L. G., and Rider, W. J.: Implicit large eddy simulation, vol. 10, Cambridge university press Cambridge, 2007.

Häfner, D., Nuterman, R., and Jochum, M.: Fast, cheap, and turbulent—Global ocean modeling with GPU acceleration in python, Journal of Advances in Modeling Earth Systems, 13, e2021MS002 717, 2021.

Harten, A.: On a class of high resolution total-variation-stable finite-difference schemes, SIAM Journal on Numerical Analysis, 21, 1–23, 1984.

Hogg, A., Blundell, J., Dewar, W., and Killworth, P.: Formulation and users' guide for Q-GCM, 2014.

Jiang, G.-S. and Shu, C.-W.: Efficient implementation of weighted ENO schemes, Journal of computational physics, 126, 202–228, 1996.

Kevlahan, N. K.-R. and Lemarié, F.: wavetrisk-2.1: an adaptive dynamical core for ocean modelling, Geoscientific Model Development, 15, 6521–6539, 2022.

Kochkov, D., Yuval, J., Langmore, I., Norgaard, P., Smith, J., Mooers, G., Lottes, J., Rasp, S., Düben, P., Klöwer, M., et al.: Neural General Circulation Models, arXiv preprint arXiv:2311.07222, 2023.

Lemarié, F., Debreu, L., Madec, G., Demange, J., Molines, J.-M., and Honnorat, M.: Stability constraints for oceanic numerical models: implications for the formulation of time and space discretizations, Ocean Modelling, 92, 124–148, 2015.

Li, L., Deremble, B., Lahaye, N., and Mémin, E.: Stochastic Data-Driven Parameterization of Unresolved Eddy Effects in a Baroclinic Quasi-Geostrophic Model, Journal of Advances in Modeling Earth Systems, 15, e2022MS003 297, 2023.

Liu, X.-D., Osher, S., and Chan, T.: Weighted essentially non-oscillatory schemes, Journal of computational physics, 115, 200–212, 1994.

Marshall, D. P., Maddison, J. R., and Berloff, P. S.: A framework for parameterizing eddy potential vorticity fluxes, Journal of Physical Oceanography, 42, 539–557, 2012.

Morel, Y. G. and Carton, X. J.: Multipolar vortices in two-dimensional incompressible flows, Journal of Fluid Mechanics, 267, 23–51, 1994.

Paszke, A., Gross, S., Massa, F., Lerer, A., Bradbury, J., Chanan, G., Killeen, T., Lin, Z., Gimelshein, N., Antiga, L., et al.: Pytorch: An imperative style, high-performance deep learning library, Advances in neural information processing systems, 32, 2019.

Press, W. H. and Teukolsky, S. A.: Numerical recipes 3rd edition: The art of scientific computing, Cambridge university press, 2007.

Proskurowski, W. and Widlund, O.: On the numerical solution of Helmholtz's equation by the capacitance matrix method, Mathematics of Computation, 30, 433–468, 1976.

Roullet, G., Mcwilliams, J. C., Capet, X., and Molemaker, M. J.: Properties of steady geostrophic turbulence with isopycnal outcropping, Journal of Physical Oceanography, 42, 18–38, 2012.

Ryzhov, E., Kondrashov, D., Agarwal, N., McWilliams, J., and Berloff, P.: On data-driven induction of the low-frequency variability in a coarse-resolution ocean model, Ocean Modelling, 153, 101 664, 2020.

Shu, C.-W. and Osher, S.: Efficient implementation of essentially non-oscillatory shock-capturing schemes, Journal of computational physics, 77, 439–471, 1988.

Uchida, T., Deremble, B., and Popinet, S.: Deterministic model of the eddy dynamics for a midlatitude ocean model, Journal of Physical Oceanography, 52, 1133–1154, 2022.

Van der Vorst, H. A.: Bi-CGSTAB: A fast and smoothly converging variant of Bi-CG for the solution of nonsymmetric linear systems, SIAM Journal on scientific and Statistical Computing, 13, 631–644, 1992.

Von Hardenberg, J., McWilliams, J., Provenzale, A., Shchepetkin, A., and Weiss, J.: Vortex merging in quasi-geostrophic flows, Journal of Fluid Mechanics, 412, 331–353, 2000.

Zanna, L., Mana, P. P., Anstey, J., David, T., and Bolton, T.: Scale-aware deterministic and stochastic parametrizations of eddy-mean flow interaction, Ocean Modelling, 111, 66–80, 2017.